# Advances in the Steady-State Hybrid Regime in DIII-D – a Fully Non-Inductive, ELM-Suppressed Scenario for ITER

C.C. Petty[1], R. Nazikian[2], J.M. Park[3], F. Turco[4], Xi Chen[1], L. Cui[2], T.E. Evans[1], N.M. Ferraro[2], J.R. Ferron[1], A.M. Garofalo[1], B.A. Grierson[2], C.T. Holcomb[5], A.W. Hyatt[1], E. Kolemen[2], R.J. La Haye[1], C. Lasnier[5], N. Logan[2], T.C. Luce[1], G.R. McKee[6], D. Orlov[7], T.H. Osborne[1], D.C. Pace[1], C. Paz-Soldan[1], T.W. Petrie[1], P.B. Snyder[1], W.M. Solomon[1], N.Z. Taylor[8], K.E. Thome[8], M.A. Van Zeeland[1] and Y. Zhu[9]

[1]General Atomics, PO Box 85608, San Diego, CA 92186-5608, USA
[2]Princeton Plasma Physics Laboratory, 100 Stellarator Rd., Princeton, NJ 08540, USA
[3]Oak Ridge National Laboratory, PO Box 2008, Oak Ridge, TN 37831, USA
[4]Columbia University, 2960 Broadway, New York, NY 10027-6900, USA
[5]Lawrence Livermore National Laboratory, 7000 East Ave, Livermore, CA 94550, USA
[6]University of Wisconsin Madison, 1150 University Ave., Madison, WI 53706, USA
[7]University of California San Diego, 9500 Gilman Dr., La Jolla, CA 92093, USA
[8]Oak Ridge Associated Universities, PO Box 117, Oak Ridge, TN 37831, USA
[9]University of California Irvine, Irvine, CA 92697, USA

E-mail contact of main author: petty@fusion.gat.com

**Abstract.** The hybrid regime with beta, collisionality, safety factor and plasma shape relevant to the ITER steady-state mission has been successfully integrated with ELM suppression by applying an odd parity n=3 resonant magnetic perturbation (RMP). Fully non-inductive hybrids in the DIII-D tokamak with high beta ($\langle\beta\rangle \leq 2.8\%$) and high confinement ($H_{98y2} \leq 1.4$) in the ITER similar shape have achieved zero surface loop voltage for up to two current relaxation times using efficient central current drive from ECCD and NBCD. The n=3 RMP causes surprisingly little increase in thermal transport during ELM suppression. Poloidal magnetic flux pumping in hybrid plasmas maintains q above 1 without loss of current drive efficiency, except that experiments show that extremely peaked ECCD profiles can create sawteeth. During ECCD, Alfvén eigenmode (AE) activity is replaced by a more benign fishbone-like mode, reducing anomalous beam ion diffusion by a factor of 2. While the electron and ion thermal diffusivities substantially increase with higher ECCD power, the loss of confinement can be offset by the decreased fast ion transport resulting from AE suppression. Extrapolations from DIII-D along a dimensionless parameter scaling path as well as those using self-consistent theory-based modeling show that these ELM-suppressed, fully non-inductive hybrids can achieve the $Q_{fus} = 5$ ITER steady-state mission.

## 1. Introduction

Steady-state operation is an important goal of the tokamak development program, but self-consistent scenarios supported by a physics basis sufficient for extrapolation to future devices do not yet exist, even for burning plasma experiments that require modest fusion energy gain. A critical mission of the ITER project is the achievement of steady-state operation through current drive with a fusion energy gain of $Q_{fus} \geq 5$ [1,2], while the mission of a fusion development facility is to develop fusion blankets and test materials with high neutron fluence in a modest-sized device with modest energy gain ($Q_{fus} < 5$) [3]. A complete scenario for such steady-state operation that coherently treats transport, stability, current drive, divertor performance and plasma equilibrium, and satisfies all relevant constraints has yet to be developed. Nevertheless, many of these individual pieces have already been demonstrated, and the focus of the tokamak development program is beginning to shift towards the task of integrating these pieces into a single discharge [4]. In addition to demonstrating integration,

the physics understanding needed to extrapolate a core-edge integrated, steady-state scenario to future burning plasma devices needs to be developed. This is especially important for aspects that cannot be truly integrated in present-day tokamaks owing to their relatively small size (for example, combining a low-collisionality H-mode pedestal with a high-density detached divertor [5]).

An exciting new development in steady-state scenario research, discussed in this paper, is the integration of edge localized mode (ELM) suppression with a fully non-inductive hybrid plasma (see Fig. 1) with beta (β), collisionality (ν*), safety factor (q) and plasma shape relevant to ITER. Experiments in the DIII-D tokamak have previously demonstrated a "steady-state" hybrid scenario using a mixture of strong central current drive and bootstrap current to achieve zero surface loop voltage for <2 current relaxation times [6,7]. Here, the "hybrid" regime refers to a stationary, high performance H-mode scenario that has higher confinement and greater stability to the m/n=2/1 tearing mode (m and n refer to the poloidal and toroidal mode numbers) than the conventional H-mode regime [8,9]. A joint report has been published from four large divertor tokamaks on the physics basis of the hybrid scenario and prospects for applications in ITER [10]. While 100% non-inductive operation was achieved in high beta ($\langle\beta\rangle = 3.1\%$) hybrids that are attractive for future burning plasma devices [6], these discharges did not incorporate any techniques, such as ELM suppression, to mitigate the divertor heat flux. Type-I ELMs cannot be tolerated in future fusion reactors owing to the large anticipated erosion and dangerous cyclic thermal stresses expected on plasma facing components [11]. Previous experiments on DIII-D [12] have demonstrated ELM suppression in low-collisionality inductive plasmas using resonant magnetic perturbations (RMP) applied by external coils, and ELM mitigation and/or control by 3D fields has been demonstrated in many devices [13]. In the experiments described in this paper, ELM suppression is achieved in fully non-inductive plasmas for the first time using novel high-beta amplification of modest-level n=3 RMP with odd parity. DIII-D has two toroidal rows of six internal coils (I-coils), one above and one below the midplane. The six coils in each row can produce an n=3 magnetic field. By odd parity we mean that the coil current in the upper row is oppositely directed to the coil current in the lower row. This parity is chosen to match to the helicity of the magnetic field lines in the plasma edge. The odd parity configuration couples well to the high-$q_{95}$ ITER steady-state case, whereas the even parity configuration couples better to the low-$q_{95}$ ITER baseline scenario. Analysis suggests that the excitation of a marginally-stable edge kink mode that is amplified at high beta together with a high density of n=3 rational surfaces in the edge of the plasma are responsible for the favorable characteristics of ELM suppression in these steady-state hybrid plasmas. It is well known that for low-n pressure driven kink modes the plasma amplifies external magnetic perturbations as beta is increased. In this study the plasma is shown to exhibit multiple stable modes, one of which is resonant at the plasma edge. Beta induced amplification of this stable edge kink mode is considered responsible for ELM suppression; the detailed physics behind the RMP ELM suppression will be discussed in a separate paper [14].

An advantage of the steady-state hybrid scenario is the self-organized nature of the plasma current profile, which should allow the discharge to survive a temporary decrease in external current drive (perhaps due to a hardware failure or a transient spike in plasma density). An important feature of the hybrid regime in DIII-D with a m/n=3/2 tearing mode is the anomalously broad current profile that maintains the safety factor minimum ($q_{min}$) slightly above 1 [15,16]. Consequently, good alignment between the current drive and plasma current profiles is not necessary as the anomalous radial transport of poloidal magnetic flux, referred to as poloidal magnetic flux pumping, self-organizes the current density profile (thus, changes in the external current drive profile have a small effect on the q profile [17]). Since the beneficial characteristics of the hybrid regime are independent of the non-inductive current

fraction [7], in the event of a drop in external current drive (but not necessarily β), the "steady-state" plasma can transparently switch over to inductive current drive from the central solenoid until fully non-inductive operation is restored. This is of large practical advantage, since for many steady-state scenarios which rely on the external control of the current profile using finely-tuned sources of current drive, even the temporary loss of such current drive systems will likely result in the early termination of the discharge as the safety factor profile evolves away from the optimal value. The hybrid scenario is even re-accessible following a total loss of heating/current drive power as experiments have demonstrated a "late heating scheme" where the hybrid regime is entered following a long ohmic, sawtoothing phase [18].

The remainder of this paper is organized as follows. In Sec. 2, the general characteristics of the steady-state hybrid scenario with RMP ELM suppression, the current drive properties and behavior of the loop voltage are examined. The stability to sawteeth and energetic particle modes to localized current drive, as well as the ideal mode stability, are investigated in Sec. 3. In Sec. 4, the thermal transport properties of these steady-state hybrids are discussed, including the effect of RMP ELM suppression and central electron heating. Finally, the extrapolation of these RMP ELM-suppressed, steady-state hybrids to ITER is discussed in Sec. 5, and conclusions are given in Sec. 6.

## 2. Current Drive in Steady-State Hybrids With RMP ELM Suppression

Experiments in DIII-D have been developing a hybrid scenario using a mixture of central electron cyclotron current drive (ECCD), neutral beam current drive (NBCD) and bootstrap current to obtain 100% non-inductive operation [6,7]. For the first time, such a "steady-state" hybrid discharge in the ITER similar shape has been successfully integrated with ELM suppression by applying an n=3 RMP from the I-coil with odd parity, as shown in Fig. 2. The ELM suppression continues during the $\beta_N$ ramp down phase until the I-coil is turned off at 6 s. MHD calculations show that the combination of a strongly-driven edge kink mode and a high density of edge rational surfaces produce an island chain that can lead to robust ELM suppression (see Ref. [14] for more details). The fully non-inductive period of the discharge, with average values of normalized beta $\beta_N$ = 3.0, poloidal beta $\beta_P$ = 1.9 and IPB98(y,2) confinement factor $H_{98y2}$ = 1.2 using 3.5 MW of ECCD power and 9.9 MW of NBCD power, is limited by the allowed neutral beam injection (NBI) duration (although for investigational purposes the ECCD is turned off 0.1 s before the NBI power ramps down). Importantly, the plasma parameters for these discharges in DIII-D extrapolate well to the expected conditions for ITER's steady-state mission (see Sec. 5). In Fig. 2(a), the bootstrap current is calculated using the Sauter model [19] and the NBCD is calculated using the orbit-following Monte Carlo code NUBEAM [20]. The linear TORAY-GA code [21-24] is used to calculate the ECCD profile, but since the quasi-linear effects are substantial (20% increase in current drive efficiency), the ECCD magnitude is enhanced to bring it into agreement with the quasi-linear Fokker-Planck code CQL3D [25]. Central ECCD plays a vital role in this steady-state scenario, driving $I_{EC}$ = 0.23 MA out of $I_P$ = 0.95 MA plasma current ($q_{95}$ = 6.6) with a current drive efficiency that is 40% higher than the neutral beams.

### 2.1. Anomalous Current Profile Broadening

A significant advantage of the hybrid scenario is that good alignment between the current profile and current drive sources is not needed owing to poloidal magnetic flux pumping, associated with a m/n=3/2 tearing mode, that raises $q_{min}$ slightly above 1 with low central magnetic shear [15,16]. This removes a trigger mechanism for the deleterious m/n=2/1 tearing mode, while the low magnetic shear is beneficial in reducing heat transport [26]. (However, comparing hybrids with and without an island at the q=1.5 surface shows that the m/n=3/2

tearing mode reduces confinement by ≈4%, which is consistent with previous DIII-D results for high-$q_{95}$ hybrids [17].) In Fig. 3, the calculated non-inductive current profile is overlaid with the measured current profile from an EFIT equilibrium reconstruction [27] constrained by the experimental pressure profile [28] and motional Stark effect (MSE) polarimetry [29]. The inductive current is negligible as the surface loop voltage is 0 ± 1 mV (averaged over 1.5 s) for this case. The measured plasma current profile is clearly broader than the sum of the driven current profiles in Fig. 3, and furthermore shows no sign of peaking over the 2.5 s high-beta phase of the discharge. The $q_{min}$ evolution for a steady-state hybrid discharge with RMP ELM suppression is compared in Fig. 4 to a simulation by the TRANSP code [30] assuming neoclassical resistivity and the calculated profiles for ECCD, NBCD and the bootstrap current; here the MSE signals used in the equilibrium reconstruction are corrected for the effect of the radial electric field using the measured plasma rotation [31]. The TRANSP modeling confirms that the experimental current profile is anomalously broad; the discharge lasts long enough (the calculated current relaxation time is $\tau_R$ = 1.9 s) for $q_{min}$ to drop well below 1 if standard current evolution is followed. While the TRANSP simulation shows an increase in $q_{min}$ at 1.7 s from the back EMF effect when ECCD is injected, this is not observed experimentally, presumably because poloidal flux pumping is already self-organizing the current profile. This poloidal flux anomaly may be consistent with the formation of an electrostatic dynamo EMF arising from the helical core equilibria [32,33].

## 2.2. Loop Voltage Response

Scans of the current drive power and poloidal beta indicate that the combination of central ECCD and bootstrap current effectively drives the surface loop voltage to zero in these hybrid plasmas, as seen in Fig. 5. For the same $\beta_P$ value, this figure shows that $V_{surf}$ (using an averaging time of 1.5-2.0 s) is lower for cases with ECCD owing to a combination of high ECCD efficiency and higher electron temperature (which increases both the NBCD and the bootstrap current). Additionally, Fig. 5 shows that overdrive of the plasma current (i.e., $V_{surf} < 0$) is observed when $\beta_P > 1.9$ in hybrids both with and without RMP ELM suppression. Table 1 compares the non-inductive currents (averaged over 2.0 s) for both a RMP ELM-suppressed hybrid with 5 gyrotrons and a similar non-RMP hybrid with 6 gyrotrons. Both of these cases are overdriven as the non-inductive currents in Table 1 add up to 0.96 MA, well above the programmed $I_P$ value of 0.90 MA. The small differences between the NBCD and bootstrap currents is mainly due to the lower density for the RMP ELM-suppressed case, which increases the former and reduces the latter. The measured loop voltage profiles from MSE-constrained equilibrium reconstructions [34,35] for these two cases are plotted in Fig. 6, verifying that the discharges are overdriven with non-inductive current (i.e., $V_{loop} < 0$) while showing that the loop voltage profiles have not quite reached equilibrium ($\tau_R \approx 1.9$ s, so the high-beta phase lasts $\approx 1.5\tau_R$ rather than the needed $>3\tau_R$).

**Table 1. Powers and currents for steady-state hybrids with and without RMP ELM-suppression.**

| | With RMP (Shot 161409) | Without RMP (shot 161414) |
|---|---|---|
| $P_{EC}$ (MW) | 3.0 | 3.4 |
| $P_{NB}$ (MW) | 10.0 | 9.5 |
| ECCD (MA) | 0.18 | 0.22 |
| NBCD (MA) | 0.55 | 0.45 |
| Bootstrap (MA) | 0.23 | 0.29 |
| Plasma Current (MA) | 0.90 | 0.90 |

Since the current profile in hybrid plasmas is anomalously broadened by poloidal magnetic flux pumping, it is reasonable to question whether the loop voltage profile remains a good indicator of the non-inductive current fraction. To investigate this, the non-inductive current ($I_{NI}$) is determined by subtracting the measured inductive current ($I_{ind}$) from the total plasma current. The inductive current is determined by first measuring the loop voltage profile [34,35],

$$V_{loop} = -2\pi \frac{\partial \psi}{\partial t},$$

Equation 1

and then using Ohm's law to find the local current density,

$$J_{ind} = -\frac{\sigma}{HR_0}\frac{\partial \psi}{\partial t},$$

Equation 2

which is integrated over area to obtain,

$$I_{ind} = 2\pi \int_0^1 J_{ind} \frac{B_{T0}^2}{\langle B^2 \rangle} \rho_b^2 \rho d\rho.$$

Equation 3

Here $\psi$ is the poloidal magnetic flux, $\sigma$ is the neoclassical conductivity, $B_{T0}$ is the central vacuum magnetic field (at major radius $R_0$), $\rho_b$ is the effective minor radius, $\rho$ is the normalized toroidal flux coordinate and $H = (R_0 B_{T0}/RB_T)\langle R^2/R_0^2 \rangle$ is a dimensionless factor that accounts for toroidal geometry. The time history of $\psi$ is determined from EFIT equilibrium reconstructions constrained by MSE data. Figure 7 plots the measured non-inductive current fraction, $f_{NI} = (I_P - I_{ind})/I_P$, versus the calculated non-inductive current fraction from TRANSP for a number of hybrid plasmas from this RMP ELM-suppressed, steady-state experiment. This figure shows that the measured $f_{NI}$ tracks the modeled $f_{NI}$ fairly well, indicating that the average value of $V_{loop}$ remains a good indicator of $I_{NI}$ in hybrid discharges. Finally, while *ad hoc* hyper-resistivity has been proposed as a possible mechanism for broadening the current profile in the hybrid scenario [36], fully non-inductive hybrids effectively rule out hyper-resistivity as playing a role in current profile broadening since it can have no effect when $V_{loop} = 0$.

Fully non-inductive hybrids with ELM suppression have been investigated with both standard $I_P$ flattop regulation and freezing the central solenoid current during flattop. A comparison of two steady-state hybrid discharges is shown in Fig. 8, the first (blue) with $I_P$ regulation and the second (red) with fixed central solenoid current from 2.5 – 5.5 s. The two plasmas have very similar current drive power, $\beta_N$, density, tearing mode activity and RMP ELM suppression. The flattop plasma current is 0.90 MA whereas the modeled non-inductive current reaches 0.95 MA (similar to the cases discussed in Table 1). Therefore, the discharge with $I_P$ regulation is overdriven, which is reflected in the persistently negative $V_{surf}$ and the central solenoid recharging. But when the central solenoid current is frozen between 2.5 – 5.5 s so that it cannot supply poloidal magnetic flux, the plasma current rises to 0.95 MA, matching the calculated non-inductive current. A difference in the $V_{surf}$ relaxation is also seen for the two cases in Fig. 8. The fast ramp up in $\beta_N$ between 1.2 – 1.6 s results in a negative surface loop voltage owing to the back EMF effect that results mainly from the rise in the pedestal bootstrap current. During this early time the loop voltage profile is far from equilibrated, however, with a positive peak around $\rho \sim 0.6$ and a negative value in the center.

On the time scale of the current relaxation time ($\tau_R \approx 1.9$ s), $V_{loop}$ equilibrates to a flat radial profile. Interestingly, while the $I_P$ regulated discharge exhibits the expected slow rise in surface loop voltage towards zero, $V_{surf}$ for the frozen solenoid current discharge equilibrates much sooner. Apparently, the rising plasma current for the latter case works to quickly flatten the $V_{loop}$ profile.

## 3. Stability Physics

While RMP ELM suppression removes one important type of plasma instability in fully non-inductive hybrid plasmas, the sawtooth instability and energetic particle modes are still observed in many situations. This section examines the behavior of these two instabilities to help us understand ways to improve the steady-state hybrid scenario. Additionally, a comparison of the experimental beta to ideal MHD limits in this section indicates that plasma response to the applied 3D fields may play an important role in ELM suppression.

### 3.1 Sawtooth Activity

Although poloidal magnetic flux pumping robustly broadens the current profile in the hybrid scenario, experiments in DIII-D find that localized current drive can affect small changes in the local current density. One example of this is the ability of localized ECCD to directly stabilize neoclassical tearing modes (NTM) by replacing the "missing" bootstrap current at rational q surfaces [37]. Figure 9 shows another example, where strong central ECCD in the RMP ELM-suppressed, steady-state hybrid scenario slightly reduces $q_{min}$ according to MSE-constrained EFIT equilibrium reconstructions. To test the effect this has on MHD activity, experiments in DIII-D have varied the ECCD current density near the plasma center using two methods: (a) a $I_{EC}$ scan at fixed deposition profile, and (b) a deposition profile scan at fixed $I_{EC}$. As shown in Fig. 10, these methods vary the peak ECCD current density by a factor of 2 to 4, with the higher current density cases being many times larger than the actual plasma current density. Considering the $P_{EC}$ scan first, increasing the peak ECCD current density with fixed profile leads to a significant increase in sawtooth activity in hybrid plasmas. As seen in Fig. 11(a), the n=1 mode amplitude and sawteeth activity are extremely weak for the lower power ($P_{EC} = 1.5$ MW) case; however, Fig. 11(b) shows that for the higher power ($P_{EC} = 3.2$ MW) case, strong sawteeth activity occurs, presumably because $q_{min}$ is pushed down to 1. The stronger sawteeth are not due to a weakening of the m/n=3/2 NTM, in fact the opposite occurs with the 3/2 mode amplitude at the wall increasing from 2.8 to 3.7 G. Interestingly, broadening the ECCD profile at fixed $P_{EC}$ lessens or even eliminates the sawteeth activity without negatively impacting the current drive efficiency. As seen in Fig. 12(a), a broad ECCD profile ($P_{EC} = 3.5$ MW) weakens the n=1 mode and essentially eliminates sawteeth, whereas a narrow ECCD profile ($P_{EC} = 3.2$ MW) strengthens the n=1 mode and generates well-formed sawteeth, as seen in Fig. 12(b). Once again, the case with stronger sawteeth has a larger 3/2 mode (4.2 G vs. 0.7 G). None of the discharges in Figs. 11 and 12 have a m/n=2/1 NTM. The appearance of sawteeth for high ECCD current density (peak magnitudes as high as ~8 MA/m$^2$) indicates that intense localized ECCD can overwhelm the poloidal flux pumping mechanism that normally keeps $q_{min} > 1$ in hybrid discharges. These results show that by tailoring the central current drive profile, some control over the plasma instabilities is possible in steady-state hybrid plasmas.

### 3.2 Energetic Particle Modes

Concurrent with the application of central ECCD in RMP ELM-suppressed, steady-state hybrid plasmas, significant weakening in Alfvén eigenmode (AE) activity is observed. Figure

13(a) shows the cross-amplitude spectrum of density fluctuations from the $CO_2$ interferometer for a hybrid plasma with only NBI. In additional to the low-frequency NTM that are ubiquitous in the DIII-D hybrid regime, a large number (8-10) of AE are observed at high frequencies (100-250 kHz). The calculated Alfvén spectral gap structure indicates these excited modes are in the frequency range for toroidal Alfvén eigenmodes (TAE) and ellipticity-induced Alfvén eigenmodes (EAE). The NBI is sub-Alfvénic as the Alfvén velocity is $\approx 6.0\times10^8$ cm/s while the beam velocity is $2.4\text{-}2.8\times10^8$ cm/s. This high-frequency AE activity disappears when either ECCD or radial ECH is deposited near the plasma center, as seen in Fig. 13(b), replaced by an intermittent energetic particle (EP) mode that is fishbone-like with toroidal mode numbers n=1-5 and rapidly chirps down in frequency [Fig. 13(c)]; the n=2 sideband strongly couples to the m/n=3/2 NTM. The physics responsible for the dramatic change in the dominant type of EP instability is still under investigation; however, a leading explanation is that the slight reduction in $q_{min}$ during central ECCD (see Fig. 9) destabilizes an n=1 fishbone, which takes over from the TAE/EAE as the dominant EP instability.

For hybrid plasmas with NBI-only heating and strong AE activity, significant beam ion transport is needed in TRANSP modeling to match the experimental neutron rate. Figure 14(a)-(d) shows that the calculated neutron rate from TRANSP without anomalous beam ion diffusion (red curve) is well above the measured neutron rate (blue curve) for hybrids without ECCD. In order to match the experimental neutron rate for the NBI-only ($P_{EC} = 0$) case, TRANSP requires a beam ion diffusion coefficient of $D_{beam} \sim 1$ m$^2$/s. The anomalous beam ion transport increases with time in correlation with higher TAE/EAE activity, as monitored by density fluctuations measured by the $CO_2$ interferometer in the 50-400 kHz band. For a similar steady-state hybrid plasma with $P_{EC} = 2.3$ MW, Fig. 14(e)-(h) shows that the experimental neutron rate is closer to the classical value and the deduced $D_{beam}$ is less than half the neutral-beam-only case. Therefore, the fishbone-like mode observed in hybrids with central ECCD is apparently more benign than the AEs in regard to anomalous beam ion transport.

An examination of multiple discharges from the steady-state hybrid experiment with RMP ELM suppression shows that the beam ion transport deduced from the neutron rate increases with stronger MHD activity in the TAE/EAE band. Figure 15 plots the value of $D_{beam}$ needed by TRANSP to match the measured neutron rate as a function of the density fluctuation amplitude measured by the $CO_2$ interferometer in a frequency band between 50 and 400 kHz (chosen to coincide with the TAE/EAE frequency band). This dataset shows that ECCD is quite effective at reducing the TAE/EAE amplitude, as previously observed in Fig. 13, and cases with and without RMP do not separate out. While for most discharges $D_{beam}$ either remains small or initially increases and then saturates, in some cases $D_{beam}$ continues to increase until the end of the discharge; in this latter situation the increasing beam ion diffusion over time correlates with higher TAE/EAE activity. An interesting feature of Fig. 15 is that the $D_{beam}$ dependence on AE amplitude suggests a critical-gradient-like threshold, with a quick ramp up from $D_{beam} \approx 0$ to $D_{beam} \approx 0.9$ m$^2$/s at the low end of the $CO_2$ amplitude scale. This behavior is reminiscent of EP experiments on DIII-D that measured critical gradient behavior of fast ion transport using beam modulation techniques [38-40].

### 3.3 Ideal MHD limits

Stability calculations show that the achieved $\beta_N$ for these RMP ELM-suppressed, steady-state hybrids equals the no-wall n=1 stability limit while remaining well below the ideal with-wall n=1 limit, as seen in Fig. 16. The theoretical stability limits are calculated by the DCON stability package [41] using EFIT equilibrium reconstructions [27] constrained by the experimental pressure profile [28], MSE polarimetry [29] and neoclassical calculation of the

pedestal bootstrap current density [42]. The no-wall limit calculated by DCON ranges from $\approx 3.1\ell_i$ early in the high-beta phase to $\approx 3.5\ell_i$ late in the high-beta phase, where $\ell_i$ is the normalized internal inductance. The ideal with-wall n=1 limit also increases slowly with time and has an average value of $\beta_N \approx 4.0$, indicating that higher beta operation should be possible in this ELM-suppressed, steady-state hybrid regime with increased heating power. Operating near the no-wall n=1 stability limit is likely a key ingredient to the success of RMP ELM suppression with modest I-coil currents in this regime. These plasmas have weakly-stable edge kink modes with positive reluctance, analogous to the Resonant Field Amplification (RFA) of stable resistive wall modes at high beta [43]. (Reluctance relates the external perturbed flux to the effective perturbed plasma current, so that positive reluctance signals amplifying modes.) In principle, the control of such weakly stable modes at high beta enables the use of small non-axisymmetric fields to achieve the resonant field amplitudes required for ELM suppression. This will be particularly important in future reactors where maximizing the plasma response will minimize the required external magnetic perturbation to achieve ELM suppression.

## 4. Transport Physics

High energy confinement is beneficial to steady-state regimes since increasing the plasma pressure raises the bootstrap current and fusion power, although confinement may be deemed "too good" if a beta limit is reached before 100% non-inductive operation is achieved. This paper highlights the favorable integration of ELM suppression with a fully non-inductive regime, but the RMP used for the former and central ECCD used in the latter can have important effects on thermal transport, which are discussed in this section. (The confinement requirements for achieving the $Q_{fus} = 5$ ITER steady-state mission in a steady-state hybrid scenario will be discussed in Sec. 5.) Furthermore, this section examines the important issue of impurity accumulation in an H-mode edge regime without ELMs.

### 4.1. Resonant Magnetic Perturbations

The odd parity n=3 RMP used for ELM suppression in steady-state hybrids has a minor impact on transport, with the strongest profile effect being a 20% drop in the toroidal rotation rate. As seen in Fig. 17, transport analysis by TRANSP using a value of $D_{beam}$ that best matches the experimental neutron rate shows that the ion thermal diffusivity increases by ≈25% for $\rho > 0.5$ when the odd parity n=3 RMP is applied. The electron thermal and electron particle diffusivities have a smaller systematic change than the ion thermal diffusivity when comparing steady-state hybrids with and without RMP at fixed heating power, with a localized increase around $\rho \sim 0.6$-0.7 paired with a decrease at larger radii. The minor impact on the local transport coefficients correlates with the small change (≈10% drop) in the global thermal confinement time during RMP application. The largest systematic transport change is in the momentum diffusivity, which increases by ≈50% at all radii with RMP. The slower toroidal rotation rate with RMP can likely be attributed to the non-resonant and resonant braking effects of non-axisymmetric magnetic fields [44].

### 4.2 Electron Heating

Central electron heating from ECCD has a more dramatic effect on the plasma profiles in steady-state hybrid plasmas. For an ECCD power scan in RMP ELM-suppressed hybrids, Fig. 18 shows that an internal transport barrier (ITB), a low transport region, is evident in the ion temperature and toroidal rotation profiles around $\rho \sim 0.5$ for NBI-only hybrids but not in hybrids with ECCD. Here, the electron density profile is measured using Thomson scattering

[45] along with four $CO_2$ interferometers, the electron temperature profile is found from a combination of Thomson scattering and electron cyclotron emission [46], and the ion temperature and rotation profiles are determined from charge exchange recombination emission of carbon impurities [47]. The carbon density also determines the effective ion charge ($Z_{eff}$) profile since carbon is the dominant impurity in these plasmas [48]. While central ECCD is effective at bringing the electron and ion temperatures closer together, above $P_{EC}$=2.3 MW the changes in the plasma profiles begin to saturate. Interestingly, the increase in bootstrap current after 5.5 s in Fig. 2(a) is due to the ITB returning after the switch off of ECCD.

Transport analysis shows that the electron and ion thermal diffusivities increase systematically with higher central electron heating, with ions having the largest increase. Transport analysis from the TRANSP code is shown in Fig. 19 using a value of $D_{beam}$ that best matches the experimental neutron rate. Both $\chi_e$ and $\chi_i$ increase with higher ECCD power at all radii (except possibly near the axis). Since $\chi_e \approx \chi_i$, using equal amounts of electron and ion heating will naturally give $T_e \approx T_i$ in these RMP ELM-suppressed hybrids. The $D_{elec}$ profile flattens during ECCD (increasing in the core and decreasing in the edge), which causes the density profile to broaden. Finally, $\chi_{mom}$ also increases during ECCD but not as much as $\chi_e$ and $\chi_i$. An important feature is that the confinement factor remains the same ($H_{98y2}$ = 1.4, calculated without including beam ion losses) for the NBI-only ($P_{EC}$ = 0) and $P_{EC}$ = 2.4 MW hybrids despite the large increase in $\chi_e$ and $\chi_i$ for the latter case. This is because the higher thermal transport during ECCD is offset by the improved beam ion transport as the TAE/EAE modes are suppressed (beam ion transport lowers $H_{98y2}$ since it reduces the neutral beam heating effectiveness). These mitigating effects appear to explain why steady-state hybrid performance responds so positively to high power ECCD, whereas for many H-mode regimes the performance noticeably decreases with higher $T_e/T_i$ [49]. If TRANSP is used to correct $H_{98y2}$ for the effect of beam ion transport, then $H_{98y2}$ decreases uniformly with increasing ECCD power, up to a 20% drop for $P_{EC}$ = 3.4 MW, tracking the changes in $\chi_e$ and $\chi_i$.

A time dependent transport analysis shows that the electron and ion thermal transport jump higher in response to central electron heating. Figure 20 plots the time history of $\chi_e$, $\chi_i$ and $D_{elec}$ at $\rho$=0.5 for three hybrids with different amounts of ECCD (same cases as in Fig. 19). The electron and ion thermal diffusivities exhibit a monotonic increase with increasing electron heating, responding quickly to step changes in ECCD power. Compared to the thermal diffusivities, the electron particle diffusivity has a weak dependence on $P_{EC}$, but this is a consequence of plotting $D_{elec}$ at $\rho$=0.5 which is a pivot point in the flattening of the $D_{elec}$ profile during ECCD [see Fig. 19(c)]. The transport coefficients plotted in Fig. 20 from TRANSP take into account the time varying beam ion transport, which is stronger than usual in these discharges; if this is not done then the transport coefficients would appear to increase steadily with time instead of being nearly constant (except when the ECCD power changes). Beam ion transport from MHD activity is also the main reason why global thermal confinement decreases over time in these hybrids. The $H_{98y2}$ factor calculated in the normal way slowly decreases during the discharge, reaching $H_{98y2} \approx 1.2$ at the highest ECCD powers (with ELM suppression), but after correcting for the increase in fast ion transport the $H_{98y2}$ factor becomes nearly constant over time. Finally, the large improvement in the thermal diffusivities after ECCD termination explains the $\beta_N$ behavior in Fig. 2(c). Towards the end of the discharge, $P_{EC}$ drops from 3.5 MW to 0 at 5.5 s, followed by the NBI power dropping from 10.0 MW to 8.0 MW about 0.1 s later. The large transport improvement after switching off ECCD results in $\beta_N$ first increasing, before decreasing in response to the NBI power drop.

### 4.3 Impurities

Impurity accumulation is another important issue for H-mode regimes without ELMs as it can lead to radiative collapse. In these experiments, short (~10 ms) puffs of $C_2F_2Cl_2$ gas are used to determine the particle confinement time of the non-recycling Cl atoms by fitting the exponential decay of the emission line measured by a VUV spectrometer. During the ELM-suppressed, steady-state phase of the hybrid discharge with $\beta_N = 3.0$, the Cl confinement time is $\tau_P = 0.20$ s, which corresponds to $\tau_P/\tau_E = 2.8$. During an earlier phase of the discharge when $\beta_N$ is being ramped up from 2.5 to 3.0, the Cl confinement time is somewhat shorter at $\tau_P/\tau_E = 1.9$. These values of $\tau_P/\tau_E$ are similar to the acceptable levels in ELMy H-modes in DIII-D [50]. Future work will compare the transport coefficients derived from time evolution of the impurity density profile to neoclassical and turbulent transport models.

## 5. Extrapolation to ITER

The fully non-inductive hybrid scenario with RMP ELM suppression discussed in this paper is a strong candidate for satisfying the ITER goal of demonstrating steady-state operation with $Q_{fus} \geq 5$, as described in reference scenario 4 ($I_P = 9$ MA, $H_{98y2} = 1.3–1.5$, $P_{fus} = 500$ MW) [51]. This section discusses two different methods of extrapolating the DIII-D steady-state hybrid regime to ITER: a dimensionless parameter scaling path and integrated theory-based modeling. The required/expected energy confinement time is an important result from these projections, both for determining whether $Q_{fus} = 5$ is obtainable and for determining whether the required current drive power and transport power balance can be simultaneously satisfied.

### 5.1. ρ* Scaling Approach

The steady-state hybrids on DIII-D with RMP ELM suppression can be projected to ITER with only a small number of assumptions. Figure 21 shows an ELM-suppressed, steady-state hybrid discharge from DIII-D scaled to ITER's major radius and magnetic field strength while keeping fixed the dimensionless parameters $\beta$, $\nu^*$ and q (i.e., $n \propto B^{4/3}R^{-1/3}$, $T \propto B^{2/3}R^{1/3}$, $I \propto BR$), as well as the plasma shape. This is essentially an extrapolation to smaller relative gyroradius ($\rho^*$) except that ITER will have a different mix of ion species and a higher thermal energy fraction (which raises the bootstrap current fraction compared to DIII-D). Note that the target DIII-D discharge is not completely stationary as increasing beam ion transport causes beta to drop ≈5% from its peak value; the energetic particles are assumed to behave classically in ITER. The electron density and temperature profile shapes on ITER are assumed to be the same as DIII-D, and the ion temperature profile is set equal to the electron [52]. The plasma current scaled to ITER is 9.6 MA, the scaled density is ≈25% above the Greenwald density [53], and the average fusion power is calculated to be 460 MW during the high-beta phase ($\langle\beta\rangle = 2.5\%$). The bootstrap current is calculated directly from the scaled plasma profiles using the Sauter model [19]. The time base in Fig. 21 is determined by multiplying the time in DIII-D by the ratio of the current relaxation times during the steady-state period ($\tau_R = 1.9$ s in DIII-D, 245 s in ITER).

The external power needed to obtain full current drive is determined using the current drive efficiencies from the ITER Physics Basis [54]. Expressed as a dimensionless efficiency $\zeta = e^3 I_{CD} n_e R/\varepsilon_o^2 P_{CD} T_e$ [55], the theoretical current drive efficiency for central ECCD (and fast wave current drive) is $\zeta_{EC} = 0.41$, while for high-injection-energy neutral beams $\zeta_{NB} = 0.52$. Figure 21 shows that ≈4.2 MA needs to be driven from external sources during the steady-state phase; for a 50-50 mix of neutral beam and RF sources, this requires a current drive power of ≈85 MW. Assuming that no additional external power is needed to obtain $\langle\beta\rangle = 2.5\%$, this gives $Q_{fus} \approx 5.4$ and $H_{98y2} \approx 1.2$ averaged over the high-beta phase. An alternative

calculation of the confinement needed to satisfy power balance in Fig. 21 can be made by recalling that this constitutes a ρ* scan from DIII-D to ITER. Ignoring the change in ion mass, plasma rotation Mach no. and thermal energy fraction, a transport scaling of $\chi = \chi_B \rho_*^{0.47}$, i.e., between Bohm and gyro-Bohm, is needed to achieve $Q_{fus} = 5.4$ in ITER based upon the DIII-D transport levels.

### 5.2. FASTRAN Simulations

Another approach to extrapolating the fully non-inductive hybrid scenario is to use integrated theory-based modeling to find an optimal set of profiles in ITER for simultaneously attaining the steady-state and $Q_{fus} = 5$ goals. An iterative numerical procedure is employed that finds a stationary solution (d/dt = 0) of core transport (TGLF [56]) using FASTRAN [57] with self-consistent calculation of equilibrium (ESC [58]) and heating/current drive sources (NUBEAM [20], TORAY-GA [21-24]). The plasma current profile used in the equilibrium reconstruction is artificially broadened to give $q_{min} = 1.05$ to be "hybrid-like". The plasma impurities are 2% Be and 0.05% Ar, and the He ash density is calculated assuming $\tau_P/\tau_E = 5$. The simulated steady-state plasma profiles from the FASTRAN modeling are shown in Fig. 22, with the global parameters given in Table 2. Interestingly, the plasma current, density, $\beta_N$ and $P_{fus}$ are close to the extrapolated values for the DIII-D discharge shown in Fig. 21. The simulation predicts that 50 MW of NBCD power and 56 MW of ECCD is needed to drive all of the plasma current, which results in a fusion gain of slightly below 5. An important prediction from the FASTRAN modeling is the confinement time, which is determined from the TGLF modeling including the effect of plasma rotation. The predicted rotation rate in Fig. 22 is likely conservative as it neglects the effect of edge intrinsic torque [59,60]. The plasma pressure at the top of the H-mode pedestal, used as a boundary condition for the TGLF modeling, is determined using EPED1 [61-64]; however, as the EPED1 pedestal height ($\beta_{N,ped} = 0.8$) is lower than the experimental value ($\beta_{N,ped} = 1.0$) for the RMP ELM-suppressed, steady-state hybrid discharges from DIII-D, the FASTRAN modeling raises the EPED1 pressure by 25%. Table 2 shows that the theory-based prediction of the confinement factor is $H_{98y2} = 1.24$, which is the same value as needed to achieve $Q_{fus} \geq 5$ for the ELM-suppressed, steady-state hybrid extrapolation from DIII-D to ITER shown in Fig. 21. If the actual EPED1 pedestal height is used, $H_{98y2}$ predicted by FASTRAN drops to 1.18, mainly due to lower ion temperature, and $Q_{fus}$ decreases to 3.

**Table 2. Projected parameters for steady-state ITER plasma shown in Fig. 22 from FASTRAN/ISP simulation.**

| | |
|---|---|
| $B_T$ | 5.3 T |
| $I_P$ | 9.5 MA |
| $n_e/n_{GW}$ | 1.14 |
| $\beta_N$ | 3.0 |
| $H_{98y2}$ | 1.24 |
| $I_{NI}/I_P$ | 1.01 |
| $I_{BS}/I_P$ | 0.56 |
| $P_{fus}$ | 487 MW |
| $P_{CD}$ | 106 MW |
| $Q_{fus}$ | 4.6 |

The FASTRAN simulations of hybrids with central current drive predict that steady-state conditions at high fusion gain can be obtained over a range of operating parameters in ITER. Figure 23 shows the predicted ITER steady-state operation space for fully non-inductive

plasmas as a function of density and current drive power. The contour lines are determined using approximately 40 FASTRAN simulations covering $7 \leq I_P \leq 11$ MA, $0.6 < n_e/n_{GW} < 1.3$ and $40 \leq P_{CD} \leq 120$ MW. Scalings for the fusion gain, non-inductive currents, etc., are then derived from these multi-dimensional scans, i.e.,

$$Q_{fus} = 0.22 I_P^{3.0} \left(\frac{n_e}{n_{GW}}\right)^{1.3} P_{CD}^{-0.85},$$

Equation 4

$$I_{NI} = 0.93 \left(\frac{n_e}{n_{GW}}\right)^{-0.08} P_{CD}^{0.54}.$$

Equation 5

The steady-state point for ITER featured in Table 2 is indicated by red circles (the contour lines do not exactly agree with the values in the table owing to the multi-dimensional fitting process). Figure 23 shows that higher $Q_{fus}$ can be obtained in steady-state plasmas in ITER by either increasing the density or the current drive power (although there is a limit to how much power ITER can handle in steady state). Even for limitations of $n_e/n_{GW} = 1$ and the "Day 1" heating/current drive power of 73 MW, $Q_{fus} = 3$ should be achievable in steady-state hybrids in ITER.

## 6. Conclusions

Experiments in DIII-D demonstrate that the hybrid scenario with ELM suppression is an attractive regime for achieving the steady-state fusion performance goals of ITER. For the first time, a high beta, fully non-inductive hybrid in the ITER similar shape is successfully integrated with ELM suppression by applying an odd parity n=3 RMP with little confinement degradation. The high current drive efficiency of central ECCD and NBCD is an important ingredient for obtaining 100% non-inductive operation in these experiments. While the loop voltage as a whole responds to increasing non-inductive current as expected, with the surface loop voltage becoming zero when $\beta_P$ reaches 1.9, the local current profile is not as predicted from standard modeling as poloidal magnetic flux pumping continues to anomalously broaden the current profile even for ELM-suppressed, steady-state conditions. The anomalously broad current profile is an important feature of the steady-state hybrid regime, as the decoupling between the plasma current profile and the current drive profile allows the latter to be located near the plasma center where the current drive efficiency is highest. However, experiments in DIII-D also show that when an extremely peaked ECCD profile is applied, the current profile broadening mechanism can be overwhelmed and sawtooth activity is observed.

The differences in transport and confinement between steady-state hybrids with and without RMP ELM suppression are fairly minor. There is little net change in the electron thermal and electron particle diffusivities, while the ion thermal diffusivity increases by ≈25% with RMP (which goes along with the ≈10% reduction in $H_{98y2}$). While central electron heating is found to immediately increase electron and ion thermal transport, it can also reduce beam ion transport by suppressing TAE/EAE energetic particle modes compared to NBI-only cases in DIII-D. These EP modes are replaced by a more benign fishbone-like instability, possibly because central ECCD depresses the minimum safety factor closer to unity (making the n=1 fishbone mode more unstable). The decreased beam ion transport can offset the increased thermal transport during ECCD, leaving $H_{98y2}$ unchanged as $P_{EC}$ is increased from 0 to 2.4 MW. Gas puff experiments show that impurity accumulation is not problematic in RMP ELM-suppressed, steady-state hybrids.

Two different extrapolation methods find that the fully non-inductive hybrid scenario with ELM suppression discussed in this paper is a strong candidate for satisfying the ITER steady-

state mission with $Q_{fus}$ = 5. Scaling a RMP ELM-suppressed, steady-state hybrid discharge from DIII-D to ITER's magnetic field strength and major radius at fixed dimensionless parameters (except ρ*) gives 460 MW of fusion power for a D-T plasma with $Q_{fus} \approx 5.4$, assuming the current drive efficiency for central ECCD and NBCD given in the ITER physics basis. A high confinement factor is not required ($H_{98y2} \approx 1.2$), rather, transport scaling intermediate between Bohm-like and gyroBohm-like is sufficient. This dimensionless parameter extrapolation is backed up by self-consistent, theory-based modeling from FASTRAN simulations that predict full current drive in a hybrid-like discharge in ITER with $Q_{fus}$ = 4.6 and $H_{98y2}$ = 1.24. Interestingly, the plasma parameters from the FASTRAN simulations are surprisingly close to the DIII-D hybrid parameters scaled to ITER. The FASTRAN simulations also show that the ITER steady-state operation space is fairly broad, with pathways to raising the fusion gain (and fusion power) by either increasing the density or current drive power.

The characteristics of RMP ELM suppression in these steady-state hybrids are consistent with strong edge kink amplification of positive reluctance modes combined with the high density of rational surfaces at the top of the pedestal. As will be discussed in a separate publication [14], these properties are quite unlike those of low-beta plasmas and the results suggest that ELM suppression by RMPs may be more effective in steady-state reactors than in present day inductive experiments.

This material is based upon work supported by the U.S. Department of Energy, Office of Science, Office of Fusion Energy Sciences, using the DIII-D National Fusion Facility, a DOE Office of Science user facility, under Awards DE-FC02-04ER54698, DE-AC02-09CH11466, DE-FG02-08ER54999, DE-FG02-04ER54761, DE-AC52-07NA27344, DE-AC05-06OR23100, SC-G903402 and DE-FC02-05ER54809. DIII-D data shown in this paper can be obtained in digital form by following the links at https://fusion.gat.com/global/D3D-DMP.

## References

[1] Aymar R. 2000 *Plasma Phys. Control. Fusion* **42** B385
[2] Shimomura Y. *et al* 2001 *Plasma Phys. Control. Fusion* **43** A385
[3] Chan V.S. *et al* 2010 *Fusion Sci. Technol.* **57** 66
[4] Luce T.C. 2011 *Phys. Plasmas* **18** 030501
[5] Ongena J. *et al* 2001 *Plasma Phys. Control. Fusion* **43** A11
[6] Turco F. *et al* 2015 *Phys. Plasmas* **22** 056113
[7] Petty C.C. *et al* 2016 *Nucl. Fusion* **56** 016016
[8] Luce T.C. *et al* 2001 *Nucl. Fusion* **41** 1585
[9] Wade M.R. *et al* 2001 *Phys. Plasmas* **8** 2208
[10] Luce T.C. *et al* 2014 *Nucl. Fusion* **54** 013015
[11] Loarte A. *et al* 2014 *Nucl. Fusion* **54** 033007
[12] Evans T.E. *et al* 2008 *Nucl. Fusion* **48** 024002
[13] Leonard A.W. 2014 *Phys. Plasmas* **21** 090501
[14] Nazikian R. *et al,* to be submitted to *Nucl. Fusion*
[15] Wade M.R. *et al* 2005 *Nucl. Fusion* **45** 407
[16] Petty C.C. *et al* 2009 *Phys. Rev. Lett.* **102** 045005
[17] Politzer P.A. *et al* 2008 *Nucl. Fusion* **48** 075001
[18] Maggi C.F. *et al* 2010 *Nucl. Fusion* **50** 025023
[19] Sauter O., Angioni C., and Lin-Liu Y.R. 1999 *Phys. Plasmas* **6** 2834
[20] Pankin A. *et al* 2004 *Comput. Phys. Commun.* **159** 157
[21] Kritz A.H., Hsuan H., Goldfinger R.C. and Batchelor D.B. 1982 *Proc. 3rd Int. Symp. On Heating in Toroidal Plasmas (Grenoble, France, 1982)* vol II (Brussels, CEC) p 707

[22] Cohen R.H. 1987 *Phys. Fluids* **30** 2442
[23] Matsuda K. 1989 *IEEE Trans. Plasma Sci.* **17** 6
[24] Lin-Liu Y.R. *et al* 1999 *Proc. 26th European Conf. on Controlled Fusion and Plasma Physics (Maastricht, the Netherlands, 1999)* vol 23J (Geneva: European Physical Society) p 1245 http://epsppd.epfl.ch/Maas/web/pdf/p3078.pdf
[25] Harvey R.W. and McCoy M.G. 1993 *Proc. IAEA Technical Committee Meeting (Montreal, Canada, 1992)* (Vienna: IAEA) p 498
[26] Kinsey J.E. *et al* 2005 *Nucl. Fusion* **45** 450
[27] Lao L.L. *et al* 1985 *Nucl. Fusion* **25** 1611
[28] Lao L.L. *et al* 1990 *Nucl. Fusion* **30** 1035
[29] Wroblewski D. and Lao L.L. 1992 *Rev. Sci. Instrum.* **63** 5140
[30] Goldston R. *et al* 1981 *J. Comput. Phys.* **43** 61
[31] Luce T.C. *et al* 2016 *Plasma Phys. Control. Fusion* **58** 125010
[32] Jardin S.C., Ferraro N. and Krebs I. 2015 *Phys. Rev. Lett.* **115** 215001
[33] Piovesan P. *et al* 2017 *Plasma Phys. Control. Fusion* **59** 014017
[34] Hinton F.L. and Hazeltine R.D. 1976 *Rev. Mod. Phys.* **48** 239
[35] Forest C.B. *et al* 1994 *Phys. Rev. Lett.* **73** 2444
[36] Casper T.A. *et al* 2007 *Nucl. Fusion* **47** 825
[37] Petty C.C. *et al* 2012 *Nucl. Fusion* **52** 013011
[38] Collins C.S. *et al* 2016 *Phys. Rev. Lett.* **116** 095001
[39] Todo Y., Van Zeeland M.A. and Heidbrink W.W. 2016 *Nucl. Fusion* **56** 112008
[40] Heidbrink W.W. *et al* 2016 *Nucl. Fusion* **56** 112011
[41] Glasser A.H. and Chance M.S. 1997 *Bull. Am. Phys. Soc.* **42** 1848
[42] Sauter O., Angioni C. and Lin-Liu Y.R. 1999 *Phys. Plasmas* **6** 2834
[43] Boozer A.H. 2001 *Phys. Rev. Lett.* **86** 5059
[44] Cole A.J., Hegna C.C. and Callen J.D. 2007 *Phys. Rev. Lett.* **99** 065001
[45] Carlstrom T.N. *et al* 1992 *Rev. Sci. Instrum.* **63** 4901
[46] Austin M.E. and Lohr J. 2003 *Rev. Sci. Instrum.* **74** 1457
[47] Gohil P. *et al* 1990 *Rev. Sci. Instrum.* **61** 2949
[48] Whyte D.G. *et al* 1997 *Nucl. Fusion* **38** 387
[49] Petty C.C. *et al* 1999 *Phys. Rev. Lett.* **83** 3661
[50] Grierson B.A. *et al* 2015 *Phys. Plasmas* **22** 055901
[51] Gormezano C. *et al* 2007 *Nucl. Fusion* **47** S285
[52] Luce T.C. *et al* 2004 *Phys. Plasmas* **11** 2627
[53] Greenwald M. *et al* 1988 *Nucl. Fusion* **28** 2199
[54] ITER Physics Basis Expert Group on Energetic Particles, Heating and Current Drive, ITER Physics Basis Editors: Chapter 6. Plasma auxiliary heating and current drive 1999 *Nucl. Fusion* **39** 2495
[55] Luce T.C. *et al* 1999 *Phys. Rev. Lett.* **83** 4550
[56] Kinsey J.E. *et al* 2008 *Phys. Plasmas* **15** 55908
[57] Park J.M. *et al* in Fusion Energy 2010 (Proc. 23rd Int. Conf. Daejeon, 2010) (Vienna: IAEA) CD-ROM file EXC/P2-05 and http://www-naweb.iaea.org/napc/physics/FEC/FEC2010/index.htm
[58] Zakharov L.E. and Pletzer A. 1999 *Phys. Plasmas* **6** 4693
[59] Chrystal C. *et al* 2017 *Phys. Plasmas* **24** 042501
[60] Chrystal C. *et al* 2017 *Phys. Plasmas* **24** 056113
[61] Snyder P.B. *et al* 2004 *Nucl. Fusion* **44** 320
[62] Snyder P.B. *et al* 2002 *Phys. Plasmas* **9** 2037
[63] Snyder P.B. *et al* 2007 *Nucl. Fusion* **47** 961
[64] Snyder P.B. and Wilson H.R. 2003 *Plasma Phys. Control. Fusion* **45** 1671

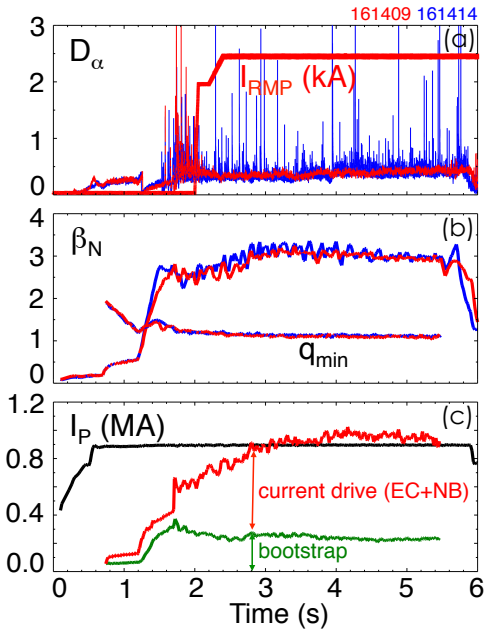


Fig. 1. Comparison of steady-state hybrid plasma with (red) and without (blue) ELM suppression: (a) divertor $D_\alpha$ light and RMP coil current, (b) normalized beta and safety factor minimum, and (c) plasma current, bootstrap current and combined external current drive for the ELM-suppressed case only.

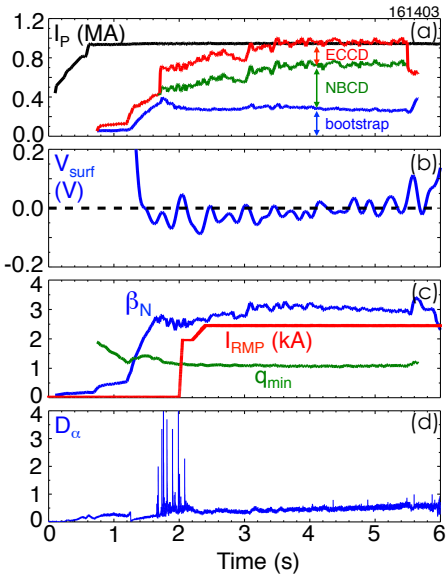


Fig. 2. Time history of steady-state hybrid discharge: (a) total plasma current and non-inductive components from ECCD, NBCD and boostrap current, (b) surface loop voltage, (c) normalized beta, safety factor minimum and RMP coil current, (d) divertor $D_\alpha$ light.

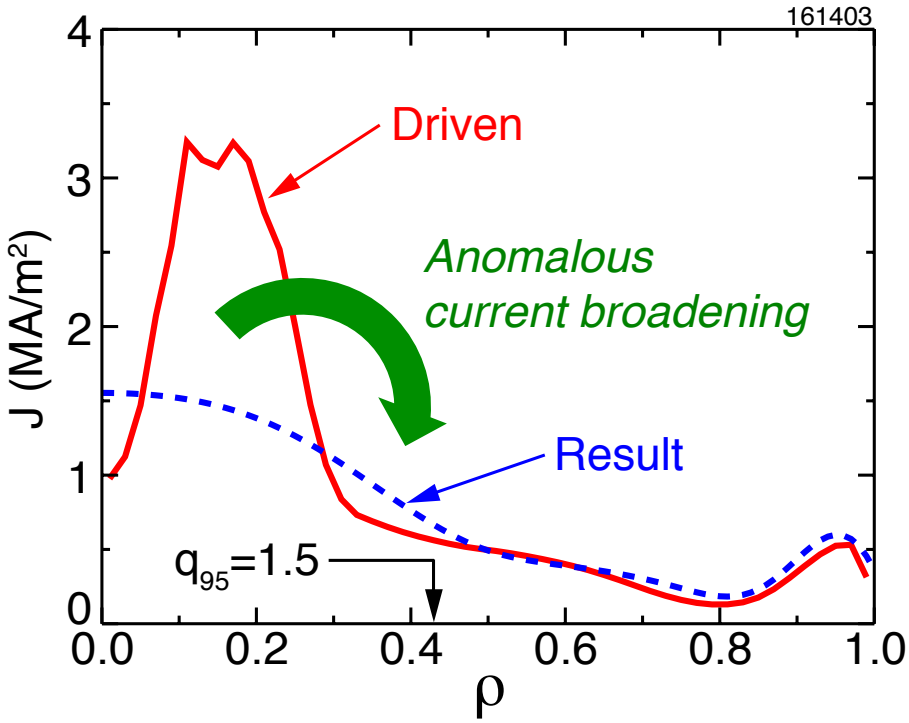


Fig. 3. Radial profiles of the calculated non-inductive current density (the sum of the ECCD, NBCD and bootstrap current), as well as the total current density from EFIT, averaged over 3.6 – 4.0 s.

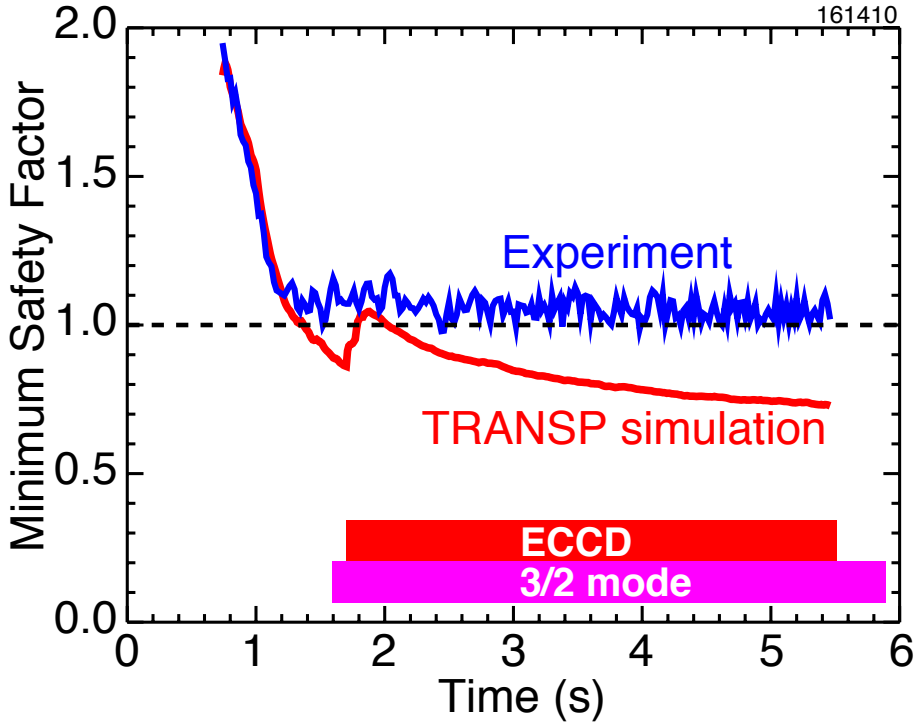


Fig. 4. Comparison of the measured $q_{min}$ with TRANSP simulation for a steady-state hybrid discharge with RMP ELM suppression.

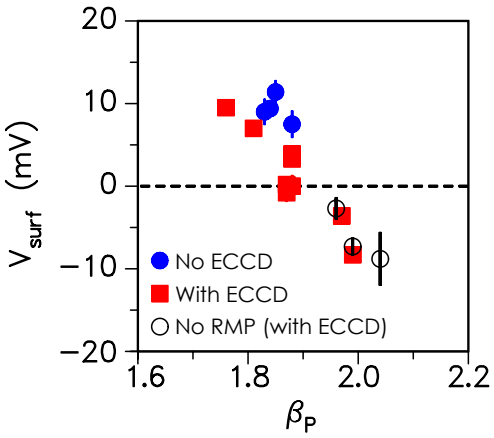


Fig. 5. Measured surface loop voltage as a function of poloidal beta for a collection of "steady-state" hybrids with RMP ELM suppression at different EC powers and plasma currents. Cases without RMP ELM suppression are indicated.

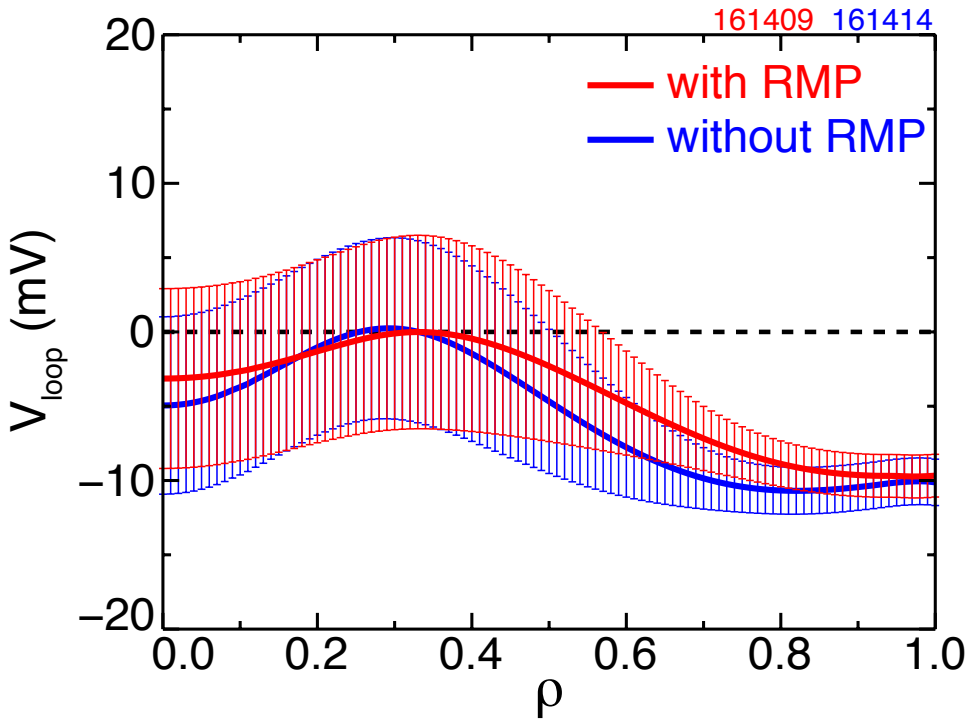


Fig. 6. Radial profile of loop voltage measured using MSE-constrained EFIT equilibrium reconstructions for steady-state hybrids with and without RMP ELM-suppression.

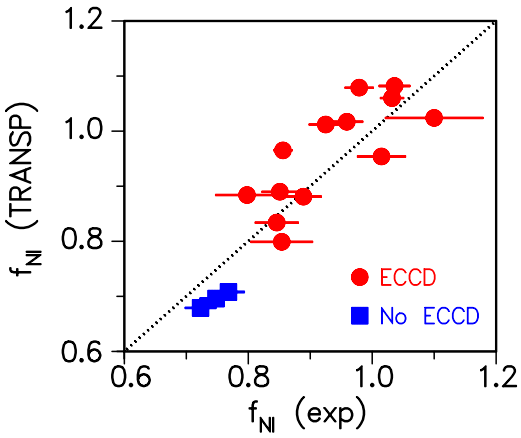


Fig. 7. Comparison of the measured and modeled non-inductive currents for hybrid plasmas taken from the “steady-state” experiment.

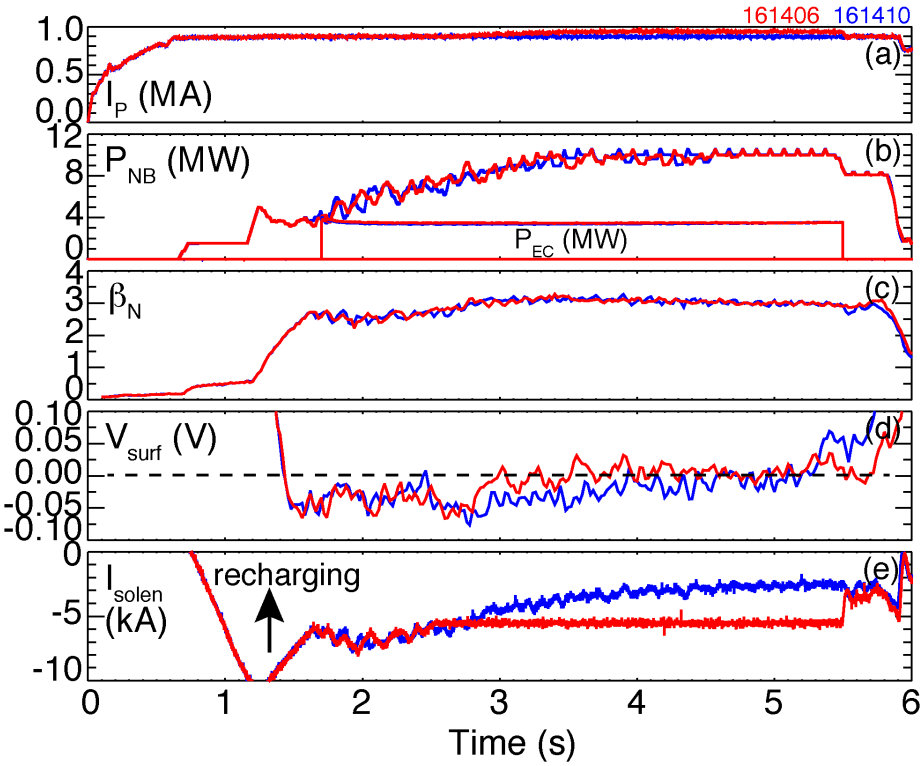


Fig. 8. Time history of steady-state hybrid discharges with plasma current regulation (blue) and central solenoid current freezing (red): (a) plasma current, (b) NBI and EC powers, (c) normalized beta, (d) surface loop voltage and (e) central solenoid current. Both plasmas have RMP ELM suppression.

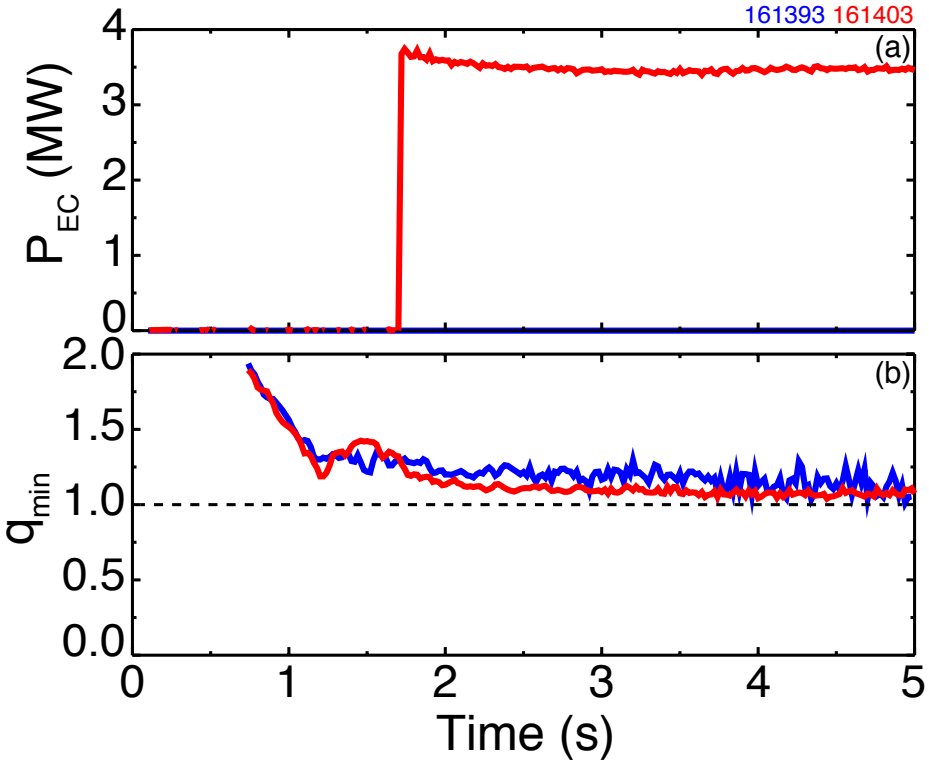


Fig. 9. Comparison of $q_{min}$ in hybrids with (red) and without (blue) central ECCD: (a) ECCD power and (b) safety factor minimum determined from MSE-constrained EFIT equilibrium reconstructions.

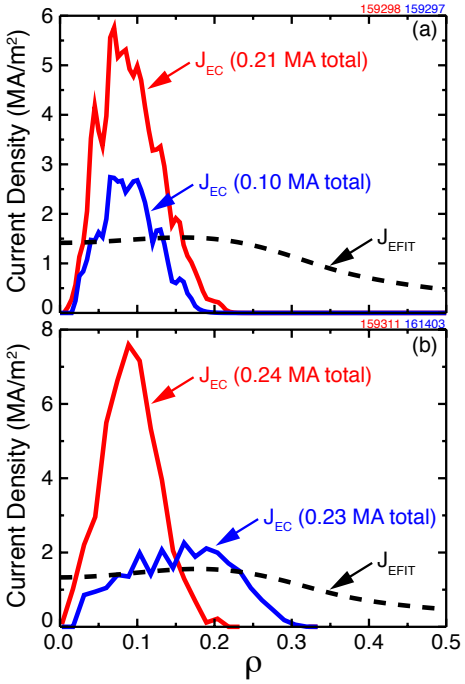


Fig. 10. Scan of ECCD current density to determine the effect on sawtooth activity in the hybrid scenario: (a) ECCD power scan at fixed deposition profile and (b) ECCD deposition profile scan at fixed power. Typical current densities from EFIT equilibrium reconstruction are also plotted.

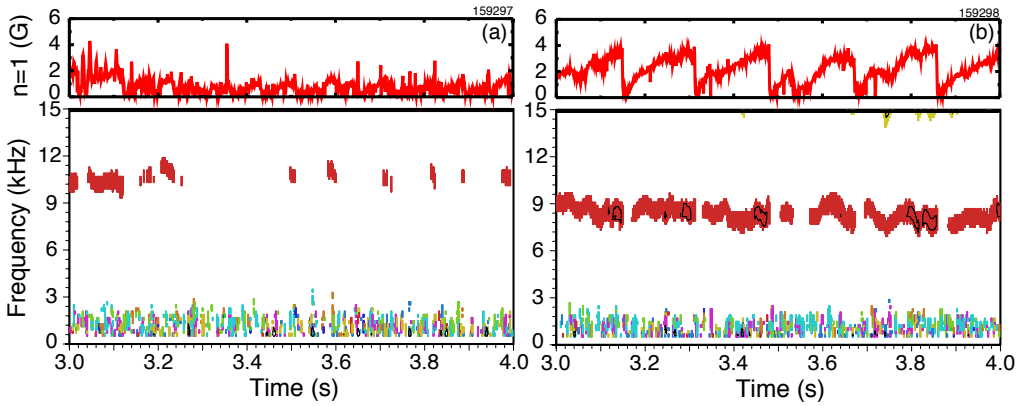


Fig. 11. Integrated n=1 mode amplitude and spectrogram for (a) the lower $P_{EC}$ case and (b) the higher $P_{EC}$ case plotted in Fig. 9(a).

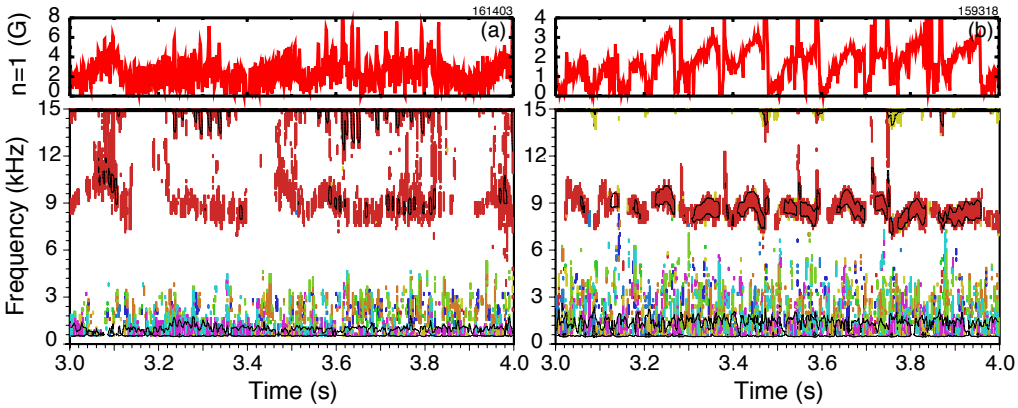


Fig. 12. Integrated n=1 mode amplitude and spectrogram for (a) the broad ECCD case and (b) the narrow ECCD case plotted in Fig. 9(b).

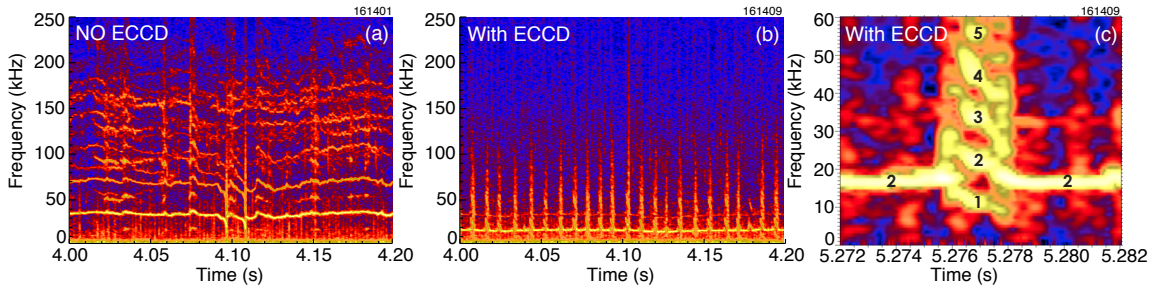


Fig. 13. Cross-amplitude spectrum of density fluctuations measured by $CO_2$ interferometer for hybrids with (a) $P_{EC} = 0$ and (b) $P_{EC} = 3.0$ MW. (c) Blowup of a single fishbone with the toroidal mode numbers indicated. The NBI power is between 9.5 and 10.0 MW.

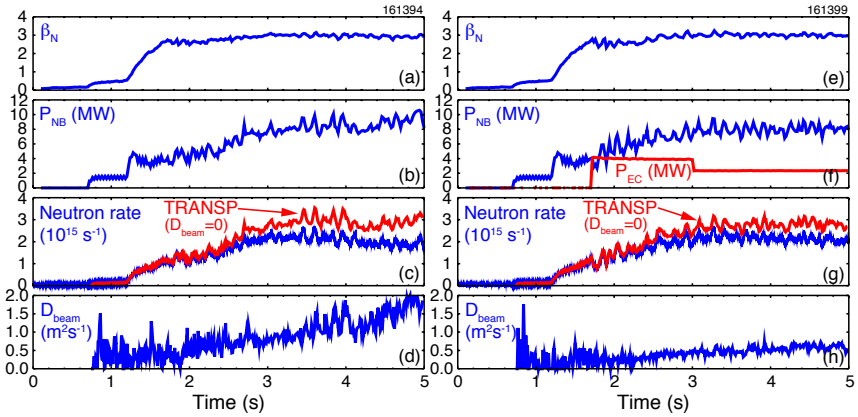


Fig. 14. (a) Normalized beta, (b) auxiliary heating power, (c) measured neutron rate (blue) and TRANSP prediction (red) and (d) beam ion diffusion coefficient ($D_{beam}$) needed by TRANSP to match experimental neutron rate for NBI-only hybrid. Panels (e)-(h) are the same except for a hybrid with ECCD and NBI.

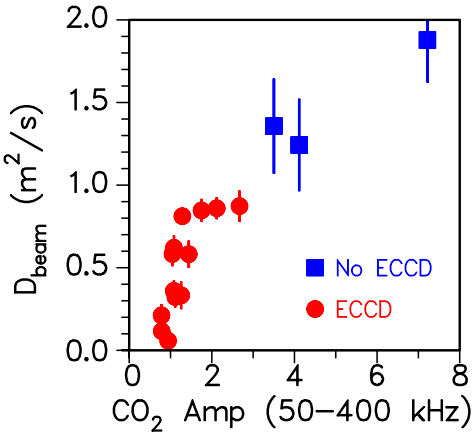


Fig. 15. Dependence of beam ion diffusion coefficient needed by TRANSP to match experimental neutron rate on the density fluctuation amplitude measured by $CO_2$ interferometer between 50 and 400 kHz.

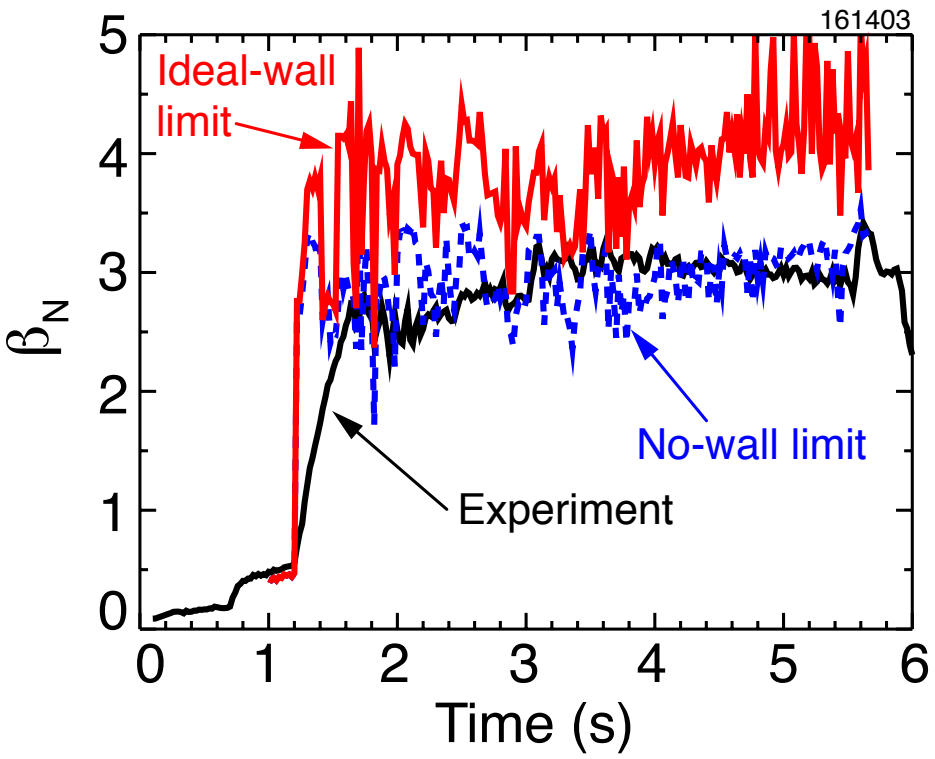


Fig. 16. Comparison of measured normalized beta for RMP ELM-suppressed, steady-state hybrid (black) with DCON calculations of the no-wall n=1 limit (blue) and ideal with-wall n=1 limit (red).

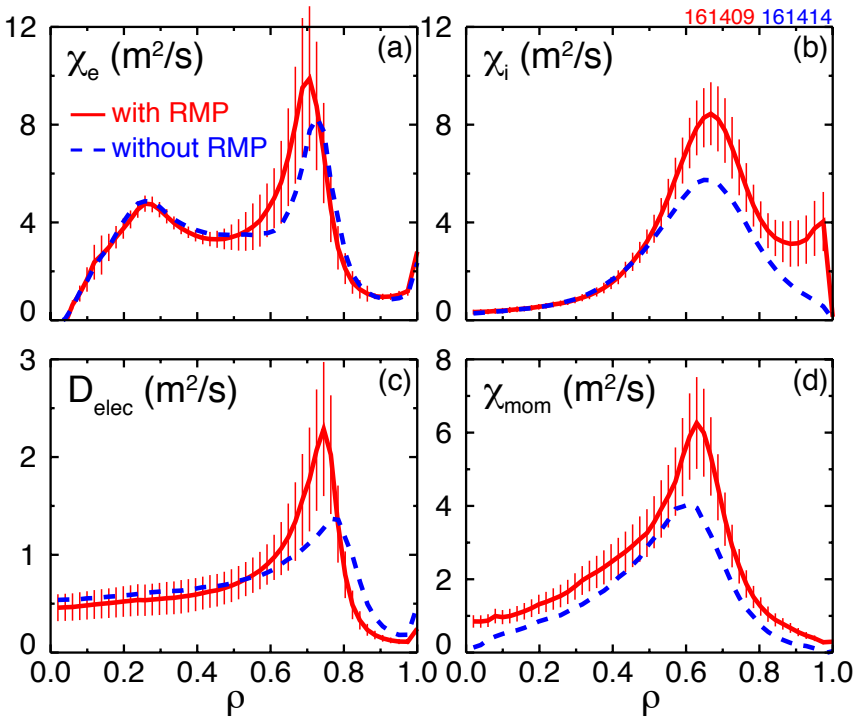


Fig. 17. TRANSP diffusivity profiles for similar steady-state hybrids with and without odd parity n=3 RMP. (a) electron thermal, (b) ion thermal, (c) particle and (d) momentum.

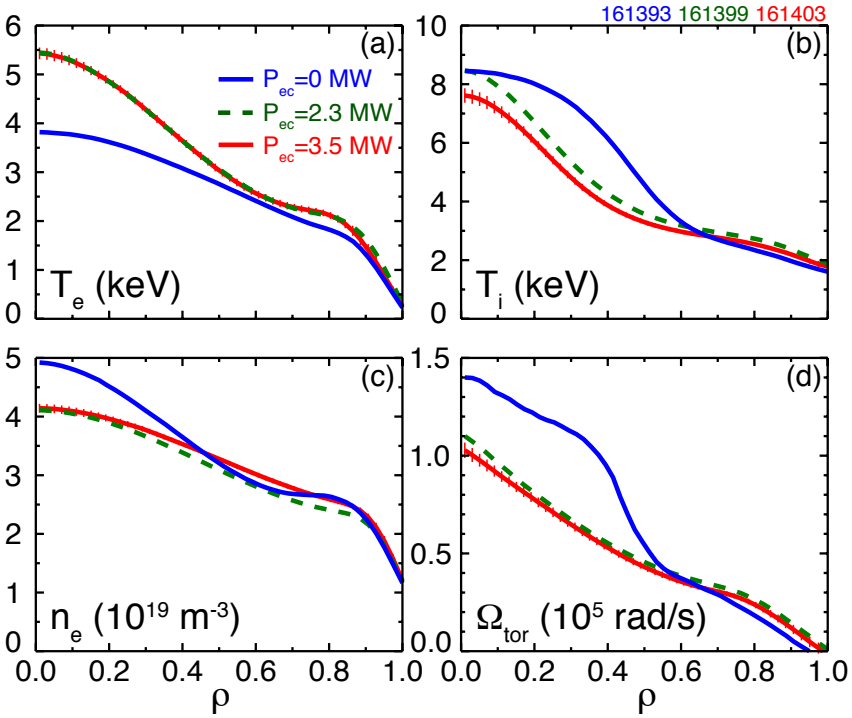


Fig. 18. Plasma profiles for RMP ELM-suppressed hybrids for different ECCD powers: (a) electron temperature, (b) ion temperature, (c) electron density, and (d) toroidal rotation.

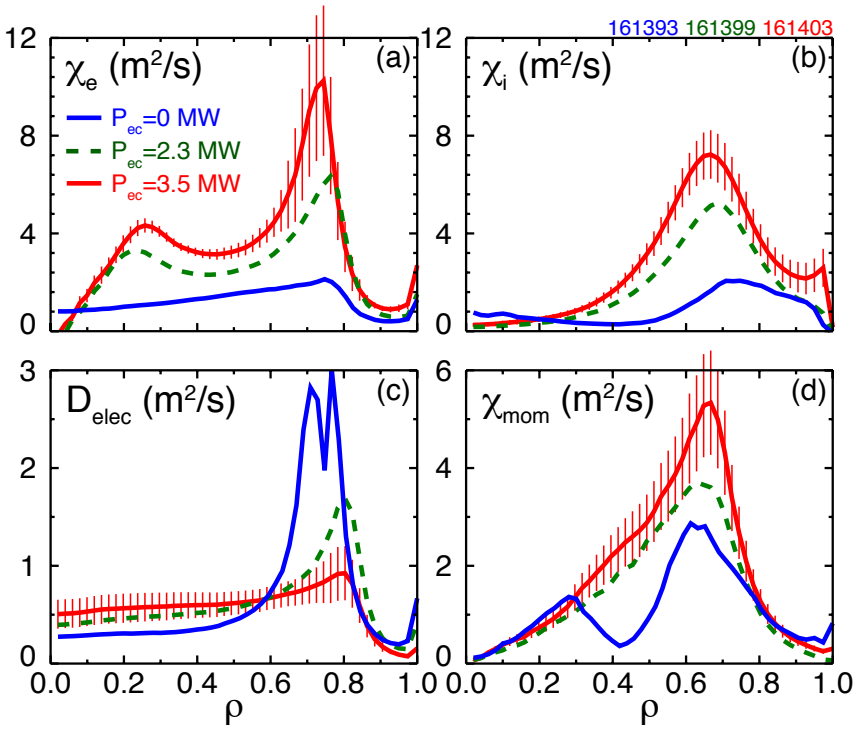


Fig. 19. TRANSP diffusivity profiles for RMP ELM-suppressed hybrids for different ECCD powers: (a) electron thermal, (b) ion thermal, (c) particle and (d) momentum.

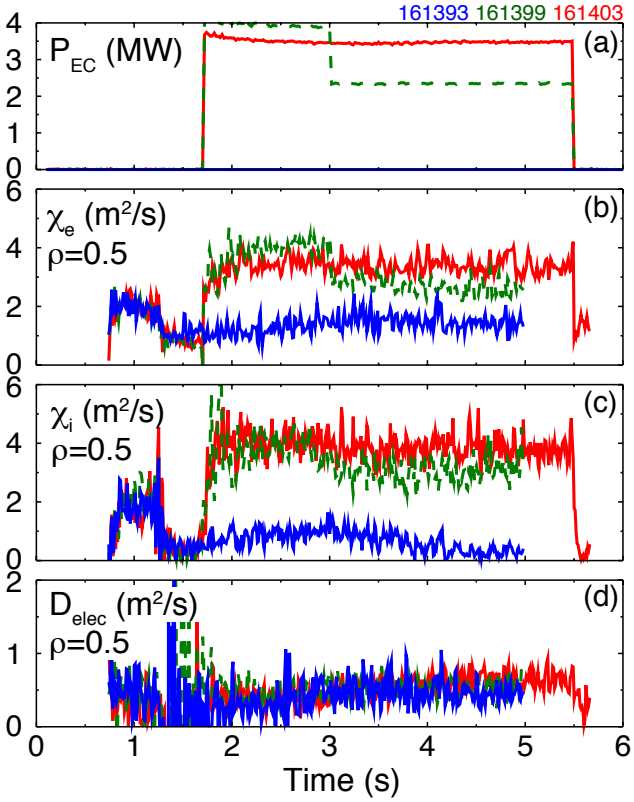


Fig. 20. Time history of TRANSP diffusivities at ρ = 0.5: (a) ECCD power, (b) electron thermal diffusivity, (c) ion thermal diffusivity and (d) electron particle diffusivity. The NBI power is between 8.0 MW and 9.9 MW.

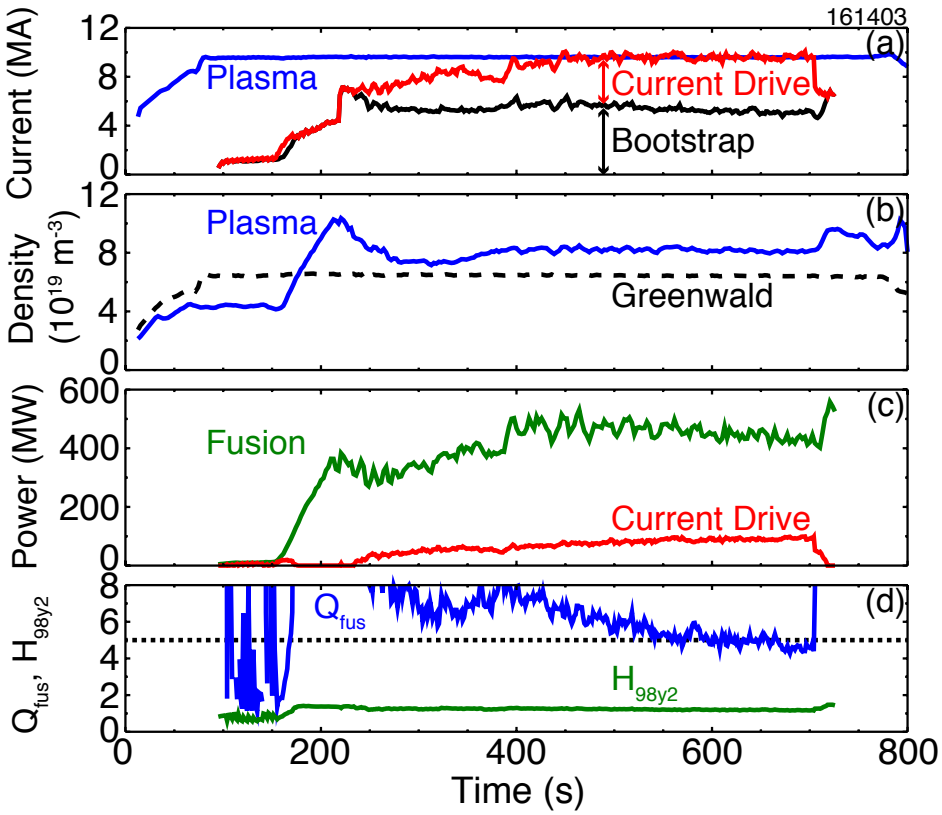


Fig. 21. ELM-suppressed, steady-state hybrid discharge from DIII-D scaled to ITER's major radius and magnetic field strength with fixed dimensionless parameters: (a) total plasma current, bootstrap current and current drive, (b) density normalized to Greenwald density, (c) D-T fusion power and current drive power, and (d) fusion gain and IPB98(y,2) confinement factor.

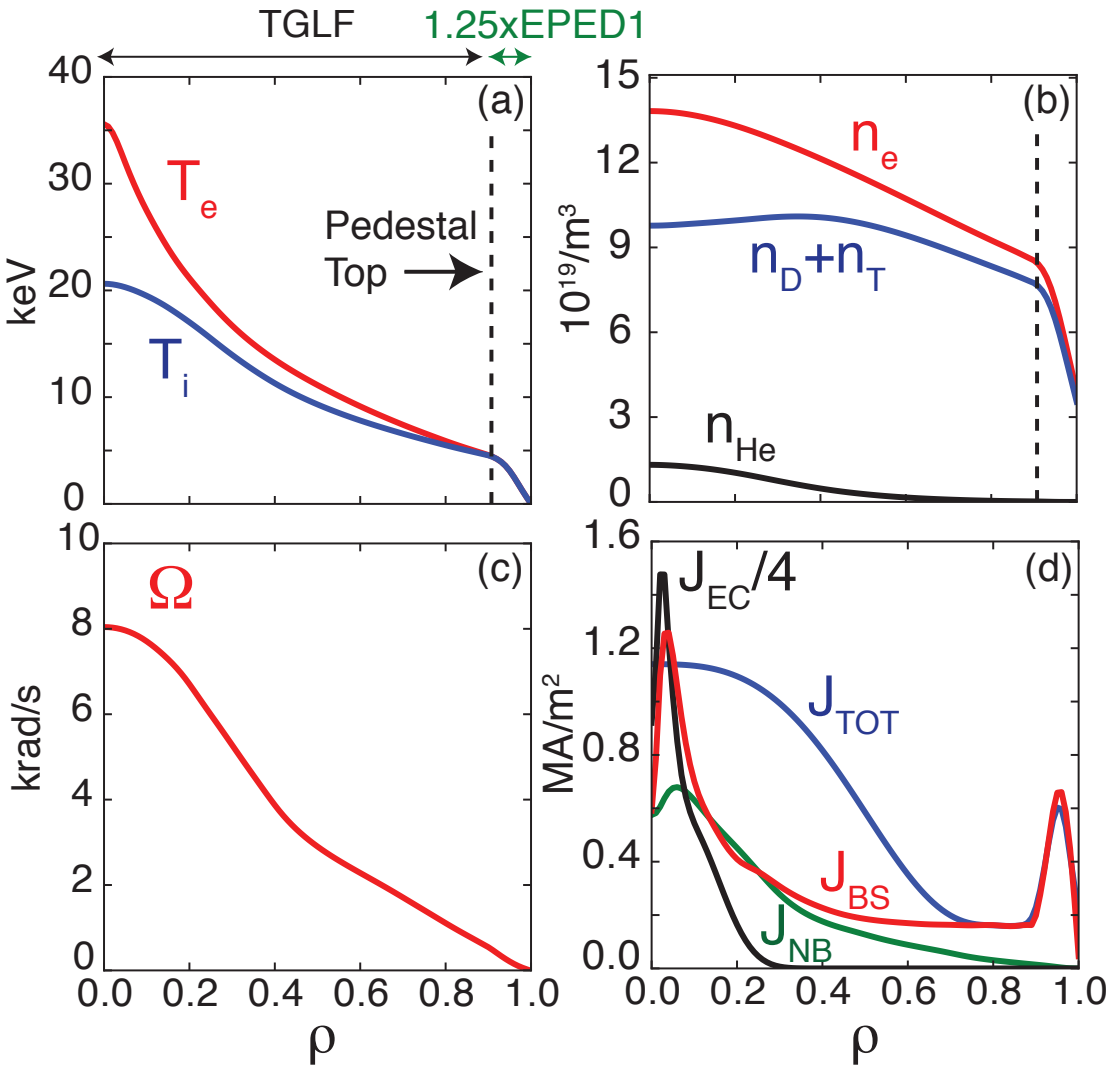


Fig. 22. Self-consistent profiles for ITER steady-state $Q_{fus} \approx 5$ case from FASTRAN simulation: (a) electron and ion temperatures, (b) electron, fuel ion and helium ash densities, (c) toroidal rotation and (d) ECCD, NBCD, bootstrap and total current densities.

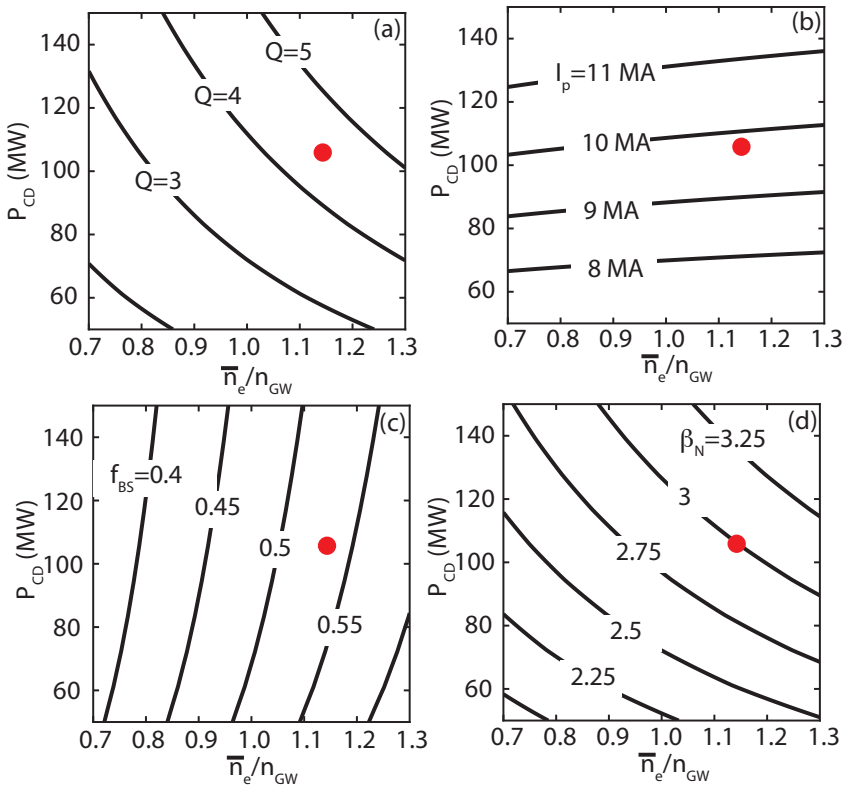


Fig. 23. FASTRAN simulation of ITER steady-state operation space as a function of density normalized to Greenwald density and current drive power: (a) fusion gain, (b) plasma current (fully non-inductive), (c) bootstrap current fraction and (d) normalized beta. Red circles indicate the ITER steady-state point from Table 2.